

Deformation mechanisms of antigorite serpentinite at subduction zone conditions determined from experimentally and naturally deformed rocks

Anne-Line Auzende, Javier Escartin, Nicolas Walte, Stéphane Guillot, Greg Hirth, Daniel J. Frost

▶ **To cite this version:**

Anne-Line Auzende, Javier Escartin, Nicolas Walte, Stéphane Guillot, Greg Hirth, et al.. Deformation mechanisms of antigorite serpentinite at subduction zone conditions determined from experimentally and naturally deformed rocks. Earth and Planetary Science Letters, 2015, 411, pp.229-240. 10.1016/j.epsl.2014.11.053 . hal-01110205

HAL Id: hal-01110205

https://hal.sorbonne-universite.fr/hal-01110205

Submitted on 27 Jan 2015

HAL is a multi-disciplinary open access archive for the deposit and dissemination of scientific research documents, whether they are published or not. The documents may come from teaching and research institutions in France or abroad, or from public or private research centers.

L'archive ouverte pluridisciplinaire **HAL**, est destinée au dépôt et à la diffusion de documents scientifiques de niveau recherche, publiés ou non, émanant des établissements d'enseignement et de recherche français ou étrangers, des laboratoires publics ou privés.

Deformation mechanisms of antigorite serpentinite at subduction zone conditions determined from experimentally and naturally deformed rocks

Anne-Line Auzende[1, now 4], Javier Escartin[2], Nicolas Walte[3], Stéphane Guillot[4], Greg Hirth[5], Daniel J. Frost[3]

[1] IMPMC, Universités Paris Diderot & Paris 06, UMR CNRS 7590, MNHN, IRD UMR 206 4 place Jussieu, F75005 Paris, France

[2] CNRS, IPGP, 1 rue Jussieu, 75238 Paris, France

[3] Bayerisches Geoinstitut, Universität Bayreuth, Universitätsstraße 30, 95447 Bayreuth, Germany

[4] ISTERRE, CNRS, Université Grenoble Alpes, 38000 Grenoble, France

[5] Department of Geological Sciences, Brown University, 324 Brook Street, Box 1846 Providence, RI 02912, USA

Corresponding author : Anne-Line Auzende

phone : +33(0)4 76 51 40 66

Email : anne-line.auzende@ujf-grenoble.fr

key words : antigorite, serpentine minerals, Deformation DIA, fluid migration, brittle, subduction zone

Abstract

Deformation-DIA experiments on antigorite serpentinite were performed at pressures of 1-3.5 GPa and temperatures of between 400 and 650°C, bracketing the stability of antigorite under subduction zone conditions. For each set of pressure-temperature (P-T) conditions, we performed two runs at strain rates of 5×10^{-5} and 1×10^{-4} s^{-1}. We complemented our study with a sample deformed in a Griggs-type apparatus at 1 GPa and 400°C (Chernak & Hirth, 2010), and with natural samples from Cuba and the Alps deformed under blueschist/eclogitic conditions. Optical and transmission electron microscopy were used for microstructural characterization and determination of deformation mechanisms. Our observations on experimentally deformed antigorite prior to breakdown show that deformation is dominated by cataclastic flow with a minor but perceptible contribution of plastic deformation (microkinking and (001) gliding mainly expressed by stacking disorder mainly). In contrast, in naturally deformed samples, deformation-related plastic structures largely dominate (stacking disorder, kinking, pressure solution), with minor but also perceptible contribution of brittle deformation. When dehydration occurs in experiments, plasticity increases and is coupled to local embrittlement attributed to antigorite dehydration. In dehydrating samples collected in the Alps, embrittlement is also observed suggesting that dehydration can contribute to intermediate-depth seimicity. Our results thus show that semibrittle deformation operates within and above the stability field of antigorite. However, naturally deformed samples record primarily plastic deformation that likely take places at low strain rates. We also document that the corrugated structure of antigorite has a control on the strain accommodation mechanisms under subduction conditions, with preferred inter and intra-grain cracking along (001) and gliding along both *a* and *b*. We also show that antigorite rheology in subduction zones is partly controlled by the presence of fluids, which can percolate within the exhumation channel via deformation-induced interconnected porosity.

1. Introduction

Subduction zones are the setting of numerous processes that impact the dynamics and geochemical evolution of the Earth (see Tatsumi & Kogiso, 2003; Hirth & Guillot, 2013). In a context where tectonic stresses dominate, the peculiar rheological properties of serpentinites focus the interest of the scientific community (see Reynard, 2013 for a review). Indeed, serpentinites are believed to be an important component of the subducting slab owing to the hydrothermal alteration of the oceanic lithosphere (Mevel, 2003; Garth and Rietbrock, 2014). Additionnally, serpentinite are present in the mantle wedge due to fluids rising from the dehydrating lithosphere, as inferred from the low seismic velocities (Hyndman & Peacock, 2003) and the high Poisson's ratio (Kamiya & Kobayasi, 2000) measured in the mantle wedge. These inferences from geophysical observations are supported by field evidence in paleo-subduction zones (Guillot et al, 2009) or serpentine mud volcanoes (Fryer et al, 1999). Understanding how serpentinites deform in subduction zones, particularly in the exhumation channel that overlies the subducting slab (Hilairet & Reynard, 2009), is of prime importance to understand decoupling between the downwelling slab and the overriding plate (Wada et al, 2008), exhumation of high-pressure rocks (Guillot et al, 2001; Agard et al, 2009), controls on fluids pathways (Padrón-Navarta et a, 2010) and, more generally, the mantle wedge dynamics (see van Keken, 2003 and references therein). Also, when serpentine breaks down at depth, the embrittlement caused by the migration of dehydration fluids is believed to trigger seismicity (Dobson et al, 2002; Hacker et al, 2003; Jung & Green, 2004; Peacock, 2001; Garth and Rietbrock, 2014). The fate of the dehydration fluids is also of great importance as they affect the properties of mantle rocks such as their rheology and melting temperature and the geochemical budget of elements that are recycled in the subduction zone (Deschamps et al, 2013; Marchesi et al, 2013).

Serpentine minerals, which are 1:1 hydrous phyllosilicates, display three main structural varieties: lizardite (flat), chrysotile (tubular), and antigorite (corrugated). In subduction zones, antigorite is the stable serpentine variety (Ulmer & Trommsdorff, 1995) and its rheological behaviour has been probed by numerous experimental studies, yielding diverging results or interpretations. Some experimental studies document deformation in the (semi-) brittle regime (Escartin et al, 1997; Jung & Green, 2004; Chernak and Hirth, 2010), while at similar deformation conditions other studies suggest that deformation operates in the plastic regime (Hilairet et al., 2007). As models of mantle wedge dynamics and fluid transport feed from these experimental data, it is necessary to better constrain and understand the precise mode of deformation of antigorite within the subduction zone, and in particular around dehydration conditions. For this purpose, we conducted experiments with a Deformation-DIA apparatus, at strain rates and total strains similar to those reported in previous studies, and coupled this experimental study with the investigation of naturally deformed samples. To facilitate the comparison of experimentally and naturally deformed rocks, we conducted experiments under P-T conditions similar to the metamorphic conditions experienced by serpentinites from the Alps and Cuba **(Figure 1)**. The microstructures of the samples described in this study (from a few µm to nm) were investigated with optical and transmission electron microscopy (TEM) to determine and interpret deformation mechanisms. Microstructural observations are indeed the key way to infer, at the micron scale, the strain accommodation processes of minerals (see Passchier and Throw, 2005), particularly for phyllosilicates (Shea and Kronenberg, 1992). Investigating both field and laboratory samples is essential in order to constrain the application field of experiments, which necessarily lack the complexity of natural systems as well as their duration. Furthermore, differences between experimental and natural microtructures should highlight the effect(s) and importance of processes not active in experiments.

2. Materials and methods

2.1. Experimental deformation

Experimental device

The D-DIA high-pressure experiments were carried out at the Bayerisches Geoinstitut (Bayreuth, Germany). This device is based on a DIA cubic anvil apparatus that consists of symmetric upper and lower blocks, four wedge-shaped thrust blocks and six anvils. The square truncations of the anvils define a cubic volume in which the high-pressure cell assembly containing the sample is loaded (**Figure 2**). The D-DIA is capable of generating pressures up to 10 GPa at high temperatures (up to 2000°C), and then deforming the sample. Hydrostatic pressure is reached at room temperature by closing up concurrently the anvils with a rate of 0.02 GPa/min. Once a high pressure is attained, temperature is increased with a heating-resistance furnace made of $LaCrO_3$, with temperature ramping up between 50 and 100°C/min. Temperature was determined using a W-Re thermocouple inserted axially into the assembly and in contact with the top of the sample. When the required P and T are achieved, the sample is annealed for a couple of hours to remove the eventual deformation-induced structures acquired during cold compression. After annealing, the samples were deformed by controlled shortening of the vertical anvil axis, which induced axial compression in the cylindrical samples while keeping the confining pressure constant. Total time at high temperature is ranging between about 180 (1×10^{-4} s^{-1}) and 240 min (5×10^{-5} s^{-1}). The deformation is monitored with displacement transducers. Strain and strain rate can thus be controlled, and are reported for each experimental run in table 1.

After quenching the sample at the end of the experiment, special care was taken to unload the sample and prevent brittle deformation structures during decompression. The retraction of the upper and lower anvils was continuously adjusted to achieve comparable

displacements to those of the four lateral anvils. For further details, the configuration of the D-DIA is described by Wang et al. (2003).

Experimental conditions are presented in **Table 1** and **Figure 1**. Pressure and temperature conditions reflect the HP-LT conditions experienced by natural serpentinites from the Monviso and Erro Tobbio Massif in the Alps (Schwartz et al, 2000; Scambelluri et al, 1995; Angiboust et al, 2011) or from Cuba (Auzende et al, 2002). They also compare well to experiments by Chernak et al (2010) conducted in a Griggs-type apparatus; Chernak et al.'s (2010) sample W1460, deformed at 1 GPa and 400°C was provided by the authors in order to conduct microstructural analyses as part of this study. The deformation experiments by Hilairet et al (2007) were performed along a colder geotherm, and included several loading and unloading cyles at different strain rates. We performed systematically two experiments under each set of P-T conditions, but at different strain-rates (see Table 1). Each sample was therefore deformed in a single deformation event at a single P and T and subsequently quenched. To document possible deformation structures induced by compression or decompression, one static experiment, DD63, was pressurized at 1.8 GPa and 550°C, annealed for two hours and then quenched and decompressed. The P-T conditions of the static experiment correspond to deformation experiments DD64 and DD65 (**Table 1**).

Starting material

The starting material was a natural serpentinite collected in the Monviso ophiolite unit (Western Alps, Italy). Originally an oceanic mantle lithosphere, the unit was buried during alpine subduction and underwent HP-LT metamorphic conditions under eclogite facies conditions. The sample, taken from a preserved lens embedded within a highly sheared matrix of serpentinites, is fully serpentinized, without trace of inherited minerals such as olivine or pyroxene (sample 627-1, see Auzende *et al.*, 2006). The serpentine chemistry lies within the

normal range of antigorite composition with little aluminium (Al_2O_3=1.97wt%) and iron (FeO_t=2.46 wt%), and the petrological investigation shows that the sample consists almost exclusively of antigorite blades up to several tens of μm in length, associated with magnetite. This sample, masssive and unfoliated at the macroscopic scale, displays under a light microscope a typical interpenetrative texture with no preferred orientation and without noticeable deformation-induced structures under a light microscope (no crystallographic preferred orientation, thereafter referred as CPO), as shown on **Figure 3a**. TEM characterisation of this sample shows crosscutting antigorite blades, displayed on Figure **3b**. Furthermore, at this nanoscale, no significant evidence of deformation was observed either.

For experiments, cylindrical cores 1.4 mm in diameter, and 1.6 mm in length were drilled in the bulk rock, and loaded in the D-DIA assembly designed for high-pressure experiments, as presented in **Figure 2a**. Materials constituting the assembly have been chosen for their physical (e.g., compression modulus) and chemical properties (no reaction with the sample) at experimental conditions.

2.2. Naturally-deformed samples

Sheared serpentinites are common in nature, but their deformation is often linked to retrograde, low P-T conditions. Instead, we have selected sheared serpentinite samples with inferred deformation occurring during prograde or peak metamorphic conditions (see Table 1), to facilitate comparison with experimental results.

Samples Cu12 and Cu24 sample were collected in the Escambray massif (Cuba) from an eclogitic unit (Auzende et al, 2002), that deformed at the metamorphic peak conditions affecting also the associated eclogitic metabasite, which shows a paragenesis consisting of almandine garnet + omphacite (Jd_{40}) ± glaucophane + phengite (Si ~3.4 pfu) + paragonite + zoisite + quartz + rutile. Sample Al24 was collected in the Erro Tobbio unit, in the alpine

Voltri massif (Italy), which records different steps of burial during subduction. Hermann et al (2000) evaluated the metamorphic conditions of unit I (labelled ET1 in Fig.1), where Al24 was collected, at P = 0.9 ±0.3 GPa and T = 360 ±60°C. Deformation structures are synchronous with prograde metamorphism. Samples Al19 and Al20 (labbeled ET3 in Fig.1) were also collected in the Erro Tobbio unit and underwent more severe metamorphic conditions, which Hermann et al. (2000) evaluate at P = 2.0 ±0.2 GPa and 600 ±40°C (ET3).

2.3. TEM observations

All samples, natural or experimental, were prepared for microstructural characterisation using an ion-polishing system, which provides for each sample large thin sections. Prior to thinning, the experimental cells were embedded in epoxy resin and cut parallel to the shortening direction with a 20µm-wire saw. The natural samples were cut perpendicular to the foliation direction. All samples were glued with Crystal Bond thermofusible epoxy onto a glass slide, thinned, and polished down to 30 µm. TEM preparations were optically selected from the polished petrographic sections. A copper slot (1 × 2 mm) was glued to surround each selected area, cored with a razor blade, and removed by heating the thermofusible epoxy. We used a conventional ion-milling system (PIPS for precision ion polishing system) with an argon beam operated at 5 kV. Electron transparency suitable for high-resolution imaging is achieved at the edge of the hole created by the milling beam. Amorphous zones were removed by decreasing the operating conditions down to 2.5 kV. TEM was performed at IMPMC (Paris, France). Imaging, diffraction and chemical data were obtained with a JEOL 2100 microscope with a LaB6 filament and a JEOL 2100F with a field emission gun, both operating at 200kV and equipped with JEOL EDX detectors. Table 2 lists and describes the deformation-related microstructures that were observed in experimentally and naturally deformed antigorite serpentinites.

3. Results

3.1. Experimental deformation

Static experiment

To discriminate between structures inherited from the starting material and those generated during compression/decompression, we examined by optical microscopy and TEM both the starting material and sample DD63, which was statically pressurized to 1.8 GPa and annealed for two hours at 550°C before temperature quenching and decompression. The petrological investigation of these two samples shows no significant differences. The original interpenetrative textures are recognized in the pressurized sample **(Figure 3c)**, which displays intercrystalline cracks that we attribute to cold decompression. TEM observations of the DD63 sample show large crosscutting antigorite blades typical of interpenetrative textures and similar to those observed in the starting material **(Figure 3b)**. A few chrysotile veins are observed in both samples, probably inherited from oceanic hydrothermal circulation or late retrogression of serpentinite 627-1 during exhumation. Based on these observations, we can assume that pressurization and depressurization do not induce changes to texture beyond the decompression micro-cracks, which remain open and are easily recognizable in the deformed samples.

Experiments without evidence for dehydration

We conducted experiments under two sets of P-T conditions within the stability field of antigorite (**Table 1** and **Figure 1**). These conditions reflect those experienced by natural serpentinites involved in subduction. We report the results obtained on our D-DIA samples and on sample W4160 provided by L. Chernak. In all samples, decompression cracks sub-perpendicular the shortening direction are observed (Figure 4b and c) and will not be taken into account when discussing the deformation-linked microstructures.

225 Observed under a polarized light microscope, the four deformed samples share several
226 features showing that deformation is not pervasive. The original interpenetrative texture is
227 well preserved and has a grain size similar to that of the starting material, with antigorite
228 blades that can reach several tens of micrometers (**Figure 4a**). None of the experimentally
229 deformed samples display penetrative foliation or schistosity. A few features associated with
230 localized deformation can however be recognized at this scale. In W1460, a sharp fault
231 crosscuts the sample at a 45° angle with respect to $\sigma_{1,}$ and has an apparent displacement of
232 about 200 µm. A second type of localization is observed in two samples (DD61, DD65), in
233 the form of narrow damaged zones (about 10 µm wide) that originate at the corner of the
234 alumina piston and propagate diagonally throughout the sample (**Figures 2d and 4b**). These
235 sheared zones propagate at an angle about 30° from σ1 in DD65 and with slightly steeper
236 angle of ~40° in DD61, and display no apparent displacement (e.g., offset at sample edge).
237 We attribute these features to an inhomogeneity of the distribution of deformation linked to
238 the impingement of the piston (stress shadows). These damage zones are not as sharp as the
239 fault observed in sample W1460 (**Figure 4c**), deformed at conditions similar to DD60 and
240 DD61. Locally, grains with significant CPO can be observed at the vicinity of the damaged
241 zones from our D-DIA samples (**Figure 4b**) and along the fault observed in W1460, as
242 previously described by Chernack et al (2010). This is not a common feature in these samples,
243 and we attribute it to the fault being locally parallel to pre-existing crystal orientation, and
244 exploiting optimally oriented grain boundaries at a local scale.

245 We conducted extensive TEM characterization of all deformed samples, and acquired
246 more than 400 micrographs, which provide a comprehensive overview of nanostructures.
247 Overall quantification of the various structures (e.g., fracture or dislocation density) observed
248 in the experimentally deformed samples is not possible, due to the inhomogeneous
249 distribution of the deformation within each sample and the great difficulty to acquire a

sufficiently large set of TEM images to perform statistical analyses. However, our systematic TEM observations do document clear microstructural patterns. According to these observations, we do not observe significant differences among samples deformed under conditions below the antigorite dehydration temperature.

Large interpenetrative blades of antigorite, similar to those in the starting material, are the most widespread texture. Decompression cracks can easily be recognized, as they are open fractures sub-perpendicular to $\sigma 1$. We also document distinctive microstructures that we can link to experimental deformation. **Figures 5a** and **b** show grains of antigorite displaying cataclastic deformation, as indicated by broken-up crystals with sharp edges, a heterogeneous grain size, and predominant delamination along the basal planes in addition to fractures at random orientations. This micro-fracturing results in local grain-size reduction and the development of incipient cataclasite textures arising from local grinding of crystals, surrounded by sample material that shows a lowr degree of deformation. These deformation textures can be observed in all samples, but are particularly common in DD60 and DD61, deformed at 1 GPa and 400°C. Further evidence of brittle behavior is the occurrence of intracrystalline fractures (**Figure 5c and d**) that affect large crystals, mainly along the cleavage planes, or associated with the bending/kinking of antigorite blades. All of these structures strongly emphasize a brittle behavior of antigorite under the P-T conditions of subduction, but at experimental strain rates that are high relative to natural strain rates.

Coupled to these brittle structures, we also observe features associated with plastic deformation, such as kinking, as shown in **Figures 5d and e** (DD60 and DD65) and in **Figure 5f** (W1460). As observed on the micrographs, gliding occurs in the basal planes along *a* or *b* directions (**Figure 5d-e** and **Figure 5f** respectivelly). As shown in the insert of **Figure 5e**, gliding along *a* is commonly accompanied by significant stacking disorder. Kinking can be associated with cracks that develop at the hinges of the kinks (F in **Figure 5d**) or with

dislocation walls that propagate within the bands (DW in **Figure 5f**). Kink-bands are observed in all deformed samples, but they are not very abundant and cannot accommodate a significant amount of the permanent strain. We also noted that in all deformed samples, most antigorite crystals are well ordered (**Figure 5g**), as observed in the starting material, with a constant modulation wavelength, and a regular layer stacking. Intracrystalline disorder (stacking faults, twinning, offset) can be recognized only in some crystals, commonly in those affected by deformation structures such as kinking (**Figure 5e** - insert), or in crystals in the vicinity, demonstrating that intra-crystalline defects are deformation-related (**Figure 5g)**. A final type of structure recognized in these samples is the local development of packets of antigorite lamellae less than 500 nm in thickness, and elongated along the direction of cleavage (**Figure 5c** for instance), similar to those observed in deformed micas (e.g., Frey and Robinson, 1999).

Experiments with evidence for dehydration

Two sets of deformation experiments were conducted under conditions above the thermal stability of antigorite (**Figure 1** and **Table 1**). Observations on the thin sections prepared from the recovered samples (DD58, DD59 and DD66) show various amounts of unreacted antigorites coexisting with small grains (<< 1µm in size) of neoformed olivine (**Figure 4d** and **e**), which is a reaction product of the antigorite dehydration (see **Figure 1**). We consider the identification of neoformed olivine as necessary and sufficient evidence of dehydration. We did not observed enstatite or chlorite (to accommodate Al_2O_3 excess in antigorite) nor "talc-like" crystals (Perrillat et al, 2005) that could be expected under these conditions; however, considering the small grain size of these new phases (a few tens of nanometers), we cannot exclude their presence. The occurrence of secondary olivine is particularly clear in DD66 (3,5 GPa, 650°C), indicating that dehydration occurred at lower temperature than that

indicated by the work of Ulmer and Trommsdorff (1995) for the corresponding experimental pressure. We thus confirm the updated curve proposed by Ulmer & Trommsdorff (1999) and also results from Hilairet et al (2006) (Figure 1). Optical observations in DD58 and DD59 show that olivine represents less than 5% in volume of the samples, meaning that the amount of released water should be very low (<0.7 vol% overall), while sample DD66 displays ~50% of neoformed olivine. The distribution of olivine is clearly restricted to narrow domains (indicated by blue arrows in **Figure 4e**), suggesting that water from the dehydration reaction was released within the areas where olivine is observed, locally increasing the water/rock ratio and pore fluid pressure.

The analysis of the recovered samples also showed that a foliation did not develop either under these extreme conditions, and that the remaining antigorite preserves the original interpenetrative texture (**Figure 4d**). However, localized domains with significant CPOs of antigorite together with olivine grains develop perpendicularly as well as obliquely (about 45°) to the compression direction, suggesting a more important contribution of plastic processes under these higher P-T conditions.

At the TEM scale, the decreased abundance of cataclastic textures in the dehydrated samples is the main difference with respect to those deformed within the stability field of antigorite, where these structures are common. Brittle structures are still present, however, and occur as microcracks that are locally decorated by neoformed grains of olivine along the open crack (**Figure 6a)**. Such repartition of the byproducts of antigorite dehydration at the edge of the crack unambiguously links this microfracturating to dehydration. The olivine grains are almost xenomorphic in shape, ranging in grain size from a few tens of nanometers to a few tens of micrometers. In these samples we also observed that plastic structures are significantly more frequent in antigorite. We observed more abundant kinking (**Figure 6b**) and an increase of both the number of disordered antigorite crystals and of the amount of intracrystalline

disorder itself within these grains (**Figure 6c**). Antigorite lamellae are also found in the samples. **Figure 6d** shows a highly strained antigorite crystal, with dislocations putatively migrating and concentrating to create dislocation walls that can evolve into new grain boundaries (subgrain formation). This process may explain the formation of antigorite packets observed in all deformed samples. Locally, we also observed lattice orientations, but no preferential orientation shared within the whole sample. Finally, in the selected region prepared for TEM investigations in sample DD66, olivine is the main phase observed, and therefore it cannot be used to constrain the deformation behavior of antigorite.

3.2. Naturally deformed samples

Petrological examination of the samples collected from the eclogitic unit of the Escambray massif in Cuba (Cu12 and Cu24) show that they consist mainly of antigorite blades, unambiguously identified by Raman spectroscopy and TEM (Auzende et al, 2004). They display a visible foliation, attributed to eclogitic deformation (**Figure 7a**). However, the antigorite blades are mostly undeformed, as shown both by the shape of the blades and the clear and uniform extinction under cross-polarized light, indicating that antigorites have massively recrystallised under eclogitic conditions. In these samples, there is no evidence of antigorite breakdown, as no olivine is observed. Serpentinite Al24 is an antigorite mylonite deformed during the first steps of the burial of the Erro Tobbio series (Unit I), under conditions close to those of experiments DD60-DD61 (Hermann et al, 2000; Auzende et al, 2006). Deformation manifests itself by the development of olivine-free shear bands (**Figure 7b**). These three samples were naturally deformed under conditions that can be related to our non-dehydrated experiments.

Serpentinites Al19 and Al20, also collected in the Erro Tobbio unit (Unit III), were also deformed during the burial of this unit, but under more severe metamorphic conditions than

those of serpentinite Al24. Indeed, they reach dehydration conditions (antigorite + brucite → olivine + water) resulting in the opening of veins filled with antigorite destabilisation products. Antigorite crystals are elongated along the foliation (**Figure 7c**). They are intensely sheared, and display undulatory extinction, characteristic of deformed crystals. This is confirmed by micrometric kink-bands visible under the light microscope. Veins filled with metamorphic olivine ± titanoclinohumite, resulting from the dehydration of antigorite, can be observed on metric outcrops (Hermann et al, 2000) as well as in thin sections (**Figure 7c**). These veins crosscut the foliation defined by the antigorite blades, and developed under eclogitic conditions that fall between those experimentally imposed for DD64-DD65 (no evidence of dehydration) and DD58-DD59 (appearance of metamorphic olivine).

At the TEM scale, we observe that natural samples display a greater amount of plastic structures (e.g., crystal disorder) compared to the experimentally deformed samples. In particular, approximately two-thirds of the crystals are highly disordered, and intracrystalline faults (stacking disorder, twinning, offset or dislocations) are very common, as illustrated on **Figure 8a and b**. This is particularly noticeable in the case of Erro Tobbio samples, where inherited antigorites have been highly sheared. In the Escambray massif samples, the density of defects in crystals is smaller. Antigorite commonly occurs as large oriented blades elongated along the foliation direction (**Figure 8e**), and display a modulation of dislocations that are scattered within the crystals, as shown on **Figure 8 b and g**. Minor chrysotile veins can be observed in most of the samples (**Fig. 8f**). In the Erro Tobbio samples it is also common to observe zones of recrystallisation at the interface between grains (**Figure 8c and d**), which were not observed in experimentally deformed samples. In a few cases we can document that the current grain boundary is a crack splitting an initial single crystal (**Figure 8d, possibly 8c**), as previously shown by Auzende et al (2006). These brittle structures, while

not widespread in the naturally deformed samples, are significant. We did not observe any cataclastic textures in any of the investigated natural samples.

The main feature that can be identified within all investigated natural samples is the amount of intra-crystalline disorder. We observed a greater amount of crystal defects in highly sheared antigorites from all Erro-Tobbio samples compared to the less-sheared antigorite sampled in Cuba. We cannot observe any clear difference between samples deformed prior to or after water release from antigorite destabilization along the subduction path.

4. Discussion

4.1. Lattice control of the deformation-induced microstructures in antigorite

Microstructures from experimentally and naturally deformed serpentinites can be used to constrain how serpentinites accommodate deformation under high-pressure conditions (i.e., subduction zone conditions). These microstructures are controlled by the crystallographic structure of serpentine, and the corrugated structure of antigorite (Figure 1-insert) likely promotes a different style of accommodation than typical to other phyllosilicates, such as lizardite (a flat serpentine variety) or micas. The brittle microstructures recognized in the investigated samples range from limited microcracking, affecting antigorite crystals (Figure 5c), to cataclastic textures (Figure 5a and b). In all cases the crystal lattice of antigorite plays a major structural role. As with all serpentine minerals, antigorite is a phyllosilicate characterized by a layered structure and weak hydrogen bonding along the basal planes (Mellini, 1982). Thus, as expected, we noted that most of the cracks propagate along the (001) cleavage direction (Figure 5) and create new grains elongated along the two other crystallographic directions, as documented in deformed lizardite (Escartin et al, 1997: Viti & Hirose, 2009) or micas (Wong and Biegel, 1985). Such morphological control of the

399 deformed antigorite crystals, coupled to solid rotation of the grains to create a shape preferred
400 orientation as a response to stress and deformation, should contribute to the strong CPO,
401 namely the *c*-axis clustering observed in naturally foliated antigorite serpentinites (van de
402 Moortele et al., 2010; Padrón-Navarta et al., 2012). Beside (001) delamination, intragranular
403 microfractures that crosscut antigorite crystals (Figure 5c) can be explained by the relatively
404 high strength of antigorite relative to other sheet silicates due to the layer reversals, with Si–
405 O–Si bonds along c^* linking the layers (Kunze, 1956; Christensen, 2004). A significant
406 proportion of these intracrystalline microfractures can be considered as features formed when
407 the limit of plasticity of the material is reached, during kinking or bending (Figure 5d). This
408 corresponds to a distinct type of intracrystalline fracturating, which can be interpreted as a
409 response to a local accumulation of stress due to the lattice accommodation of the kinking.
410 Indeed, kinking is characterized by migrating dislocations that increase the internal strain
411 energy in the antigorite crystal (see Passchier and Trouw, 2005).

412 A distinct type of microcracks can unambiguously be attributed to dehydration of
413 antigorite, as clearly established from figure 6a. These microcracks could be ascribe to
414 hydraulic fracturating as proposed by Dobson et al (2002) as well as to antigorite
415 embrittlement at the onset of the antigorite to olivine dehydration reaction (Jung et al, 2004).
416 Both process, while different, produce faulting and might be responsible for seismicity in
417 subduction zones (Raleigh & Paterson, 1965; Peacok, 2001; Hacker et al, 2003; Omori et al,
418 2004; Perillat et al, 2005). While we can hardly discuss further this issue, our results are
419 similar, at smaller scale, to the observation reported by Jung et al (2004), who observed
420 dehydration products of antigorite decorating surface of faults generated at high pressure.
421 They suggested on this basis a weakening of the structure leading to faults initiating from the
422 point where the reaction started and propagated. Fluids were evacuated while solid residue
423 remained in place. Similar conclusions were proposed by Schubnel et al (2013) from the

germanate olivine to spinel transition, with fractures initiating at the onset of the reaction. On the other hand, dehydrated Erro Tobbio serpentinites show large olivine veins crosscutting antigorite foliation, supporting fluid-induced vein opening. While microfractures can also be observed in natural samples (Figure 8), they are largely healed and display evidence for recrystallization, making it difficult to systematically recognize them, and nearly impossible to attribute them to any specific deformation process. A recent paper by Chernak & Hirth (2011) proposes that weakening during dehydration is progressive and does not imply stick-slip instabilities required to explain seismicity. While our results show that dehydration and brittle behavior are clearly linked, we provide that the observation of the dehydration-induced microcracking alone does not necessitate that brittle deformation was unstable.

Plastic microstructures are also strongly controlled by the crystal structure of antigorite. Mainly, the (001) basal plane of antigorite, although reinforced by the strong Si-O-Si bonding between the layers at reversals, remains a weak plane that is likely to be the main slip surface. Thus, as expected for a phase with a preferential slip plane, antigorite develops kink bands (Figure 5 d to f). Kinking is well documented in the semibrittle deformation of talc close to dehydration conditions (Escartin et al, 2008) and is a common feature of phyllosilicate deformation (Paterson and Weiss, 1966; Shea and Kronenberg, 1992; Anderson, 2012). Recognized kink bands clearly show that basal slip can occur along both the *a* and *b* directions (Figure e and f respectivelly), meaning that two slip systems, (001)[010] and (001)[100], may be activated during the deformation event. Previous studies have proposed the dominant activation of either a single slip system of the latter (Hirauchi et al, 2010; Bezacier et al, 2010; van de Moortele et al, 2010) or of both (Padrón-Navarta et al, 2012), based on observations of CPO in naturally sheared serpentinites. Our study confirms that both slip systems are activated. Evidence for plastic gliding of the basal plane is also provided by the development of stacking disorder. Indeed, intracrystalline disorder in antigorite crystals

such as the occurrence of microtwinning, offsets, or other stacking faults, are mostly associated with glide of the (001) plane along *a* (Table 2). Finally, in naturally deformed samples, we observed recrystallization of antigorite, as previously reported by Auzende et al (2006). Recrystallization is attributed to a pressure solution process and has recently been confirmed by Padrón-Navarta et al. (2008; 2012) and Amiguet et al (2014) in naturally sheared serpentinites. Such a mechanism can accommodate deformation very efficiently, and is not directly controlled by the structure of antigorite, but by the porosity. However, as we discussed in the previous section, microcracking and the resulting porosity of antigorite serpentinite is largely controlled by its crystal structure, which indicates that pressure solution will also promote CPO in deformed serpentinites. This is in agreement with the conclusions of Katayama et al. (2009) who assume that the recorded seismic anisotropy parallel to the subduction trench is due to serpentine that deforms and generates geophysically observable CPO, although the authors infer dislocation creep as main deformation mechanism.

4.2. Semibrittle deformation and the influence of dehydration on plasticity

The reported observations of experimentally and naturally deformed serpentinites clearly show the coexistence of both brittle and plastic deformation microstructures, pointing to a semi-brittle deformation regime for serpentinites under subduction zone conditions. At high pressure conditions, and within the stability field of antigorite, the significant proportion of highly fractured antigorite grains in the experimental samples suggests that most of the strain is accommodated by cataclastic deformation, and that plastic deformation only accommodates a small fraction of strain through basal gliding. Our results are in agreement with Chernak et al. (2010) who documented semibrittle deformation of antigorite at conditions relevant to subduction, as they reported faults and kink bands throughout their samples up to high temperature. Jung et al (2009) also detected acoustic emission characteristic of brittle

deformation within the stability field of antigorite; their samples were initially faulted and acoustic emissions were attributed to repeat frictional sliding along these preexisting faults. Here, we have confirmed these observations through the characterization of sample W1460, deformed at 1 GPa and 400°C, in which we recognized kink bands together with brittle features in the form of sample-scale faults accommodating a displacement of ~200 micrometers, a type of localized deformation lacking in our D-DIA samples. We posit that our experiments document the same type of antigorite deformation described by Chernak et al. (2010), even though our samples did not display significant localization, probably due to differences in experimental set up, inhomogeneous deformation distribution, or both. We can also compare our results with those of Hilairet et al. (2007) from deformation of an antigorite sample under subduction zone conditions in a D-DIA apparatus. These experiments were conducted at similar strain rates but to a slightly lower total strain, and at 4GPa and 400°C, as they considered a colder geotherm (see Figure 1). Hilairet et al. (2007) discussed deformation mechanisms based on stress-strain curves obtained *in situ* with x-ray synchrotron analyses, and fitted their data with a dislocation creep power law. They assumed that antigorite accommodated deformation plastically, based on the absence of stress drops and on the apparent homogeneous deformation of the sample. While their data are consistent with an effective flow law, our microstructural observations suggests that this behaviour is likely not purely plastic, but attributable to distributed semibrittle deformation, with an important component of brittle deformation. Under these conditions strain localization is not efficient and deformation may proceed without significant stress drops. Also, as antigorite only has two easy slip systems - (001)[010] and (001)[100], it does not satisfy the von Mises criterion that requires five independent slip systems for plastic flow to occur homogeneously (von Mises, 1928). Thus, deformation by dislocation creep can hardly accommodate the total strain imposed on the samples, and requires other deformation mechanisms, as indicated by Padrón-

499 Navarta et al. (2012). Our conclusions are also consistent with the results by Escartin et al.
500 (1997) who deformed antigorite under low-grade conditions (from 50 MPa to 1 GPa and
501 room temperature) relevant to deformation of the oceanic lithosphere. The results from our
502 study further support that deformation of antigorite from the subduction initiation down to
503 antigorite breakdown depths (about 150 km) occurs in the semibrittle regime.
504 At conditions above the thermal stability of antigorite, we simultaneously observed an
505 increase of plastic structures (greater intracrystalline disorder, recrystallization) together with
506 a change in the nature of the brittle features. Indeed, cataclastic structures are lacking in
507 dehydrating serpentinites and in several instances microcracks can unambiguously be linked
508 to dehydration (Figure 6a). Although only a very small amount of H_2O was released in the
509 DD58 and DD59 samples due to dehydration, water locally promoted both plastic and brittle
510 behaviour. We assume that while dehydration process promotes brittle behavior, as discussed
511 in the previous section, aqueous fluid saturation together with higher temperature may have
512 enhanced plasticity, as, for instance, previously observed in olivine (Mei and Kohlstedt, 2000;
513 Jung and Karato, 2001). This plasticity manifests through higher crystal disorder of inherited
514 crystals and recrystallisation due to pressure solution. While pressure solution is a direct
515 result of water saturation, intracrystalline disorder should also be strongly enhanced by higher
516 temperatures. We converge with Padrón-Navarta et al (2008) as they have also documented
517 an increase of intracrystaline disorder in dehydrating antigorite from Cerro del Amirez and
518 efficient pressure solution. The coexistence of brittle and plastic structures is also documented
519 in dehydrating lizardite, as documented by Viti and Hirose (2009). This apparently diverges
520 from the interpretation of Chernak and al. (2010) as they do not report brittle features in their
521 samples deformed above antigorite breakdown. However, as we did not observed significant
522 localization in our experimentally deformed samples displaying brittle microstructures, we

assume that a TEM investigation on Chernak's dehydrated samples may potentially reveal microcracks similar to those that we have observed.

4.3. Permeability and fluid migration in subduction zone

A recent experimental study by Kawano et al (2011) has shown that antigorite serpentinite, under low confining pressure (50 MPa) at low temperature, and without deformation, has a very low permeability, among the lowest of metamorphic rocks, but noted a significant anisotropy of the permeability: 10^{-22} m^2 when measured perpendicular to the foliation, and two orders of magnitude higher (10^{-20} m^2) when measured parallel to it. We have shown that deformation at high pressure, under conditions relevant to subduction zones, produces microcracks and therefore porosity mostly along the basal planes of antigorite, likely as mixed-mode I-II microcracks (Escartin et al., 1997), and we thus expect that permeability would be greatly increased in the plane defined by cleavage, and that fluid circulation may be controlled by this anisotropic permeability structure. Indeed, this porosity can be interconnected, as microcracks should align in the same directions due to rigid rotation of the grains as response to the stress. This is supported by several studies that have shown that basal planes of antigorite are aligned with the foliation of natural serpentinites (van de Moortele et al, 2010; Padrón-Navarta et al, 2012). In subduction zones, Katayama et al (2009) propose that the observed trench-parallel anisotropy is due to serpentine deformation that results in antigorite basal cleavage (and foliation) is parallel to the suduction plane. Thus, oriented microcraking will enhance the percolation of aqueous fluids along the foliation direction (**Figure 9**), as suggested in prior studies (e.g., Escartin et al., 1997; Kawano et al., 2011). Also, intragranular microcracks observed in experimentally and naturally deformed samples (Figure 5c and 8d respectively) can allow fluid migration in directions across the foliation, and thus across the deformation zone (Figure 9).

548 In subduction zones, highly deformed serpentinites are commonly recognized in the
549 serpentine channel above the subducting slab (e.g. Guillot et al, 2009). Katayama et al (2009)
550 support this statement and emphasize the preferred orientation of antigorite crystals above the
551 subducting slab, along the trench. Our results support the hypothesis that fluids likely migrate
552 within the serpentinites, consistent with evidence for aqueous fluid percolation through these
553 rocks, which include chrysotile veins as in Figure 8d (e.g., Andreani et al, 2007), and
554 evidence for pressure solution as in Figure 8c (e.g., Auzende et al, 2006; Padrón-Navarta et al,
555 2012). Geochemical observations also point toward aqueous fluids in the subducting
556 serpentinites. Indeed, Deschamps et al (2013) proposed that the observed enrichment of light
557 rare earth elements in subducted serpentinites could be ascribed to sedimentary-derived fluid
558 interacting with rock within the subduction channel after the serpentinization. Thus, all these
559 observations suggest that in spite of low permeability measured experimentally at the sample
560 scale and under static conditions (Kawano et al, 2011), aqueous fluids in the subduction
561 system seem to rather efficiently percolate in the serpentinite. This percolation likely allows
562 the development of the thin hydrated serpentine layer above the subducting slab due to the
563 buoyant ascent of the fluids via an oriented connected porosity network (i.e., along the
564 foliation), and also leading to the hydration of the mantle wedge through water transport
565 across the foliation of the deformation zone (Figure 9). This across-foliation water transport is
566 likely to be significantly less efficient than the along-foliation, owing to the nature of brittle
567 deformation processes described above, and operate throughout the subduction zone.
568
569 *4.4. Input of the comparison between Nature and experiments on deformation of antigorite*
570 *during subduction*
571 All our observations of natural and experimental samples indicate that antigorite
572 serpentinites deforms in the semibrittle regime up to its complete dehydration. Optically, the

main difference between naturally and experimentally deformed antigorite serpentinites is the presence of a penetrative foliation in the former that was induced by deformation, which is not observed in experimental samples. Yet, at the TEM scale, both types of samples reveal both brittle and plastic structures. In experiments conducted within the stability field of antigorite, it has been shown that cataclastic flow controls the rheological behaviour of serpentinite, while microstructures in natural samples instead suggest a significant contribution of plasticity, with a foliation indicative of more homogeneous deformation. The absence of foliation and lesser contribution of plasticity in experimental samples can surely be attributed to i) the higher strain rates during experimental deformation (5×10^{-5} and 1×10^{-4} during D-DIA experiments compared to 10^{-12} - 10^{-14} s^{-1} in nature), ii) to the limited strains achieved in experiments that do not allow a steady state flow (a few percent shortening in the laboratory and extremely high values in the field), as stated by Chernak et al (2010), and iii) to the absence of fluids promoting syntectonic growth that likely takes place in natural shear zones within the subduction zone. Also, most experimental samples are deformed in axial compression while natural samples are typically deformed under simple shear. This means that experimental results cannot be used to constrain the conditions under which this foliation develops in nature, as such processes cannot be replicated in laboratory experiments at the moment. Nonetheless, while low strain rates may be responsible for foliation developement, we assume that brittle features recognized in natural samples can be attributed to higher strain rates events that may or may not have a seismic origin, as stated by Chernak & Hirth (2011).

The presence of aqueous fluids derived from the dehydration of other hydrous phases during burial (see Poli and Schmidt, 1998) in natural samples subducted and exhumed under conditions below antigorite breakdown can be suggested by the presence of chrysotile veins (Figure 8b) or indication of pressure solution evidence (Figure 8c), as both structures require the presence of fluids. The significant amount of plastic microstructures in natural samples

598 can also be promoted by the presence of aqueous fluids together with higher temperature,
599 even under conditions below antigorite breakdown. This is supported by the greater amount
600 of plastic structures in experimentally dehydrated samples. We thus conclude that brittle
601 deformation in subduction zones is likely associated with high strain-rate events such as
602 deformation associated with seismicity, ocurring from throughout the subduction zone from
603 the surface to the depth of antigorite breakdown. Plastic deformation developing foliation
604 likely occurs at lower strain rates and under water saturation. Semi brittle deformation of
605 antigorite can thus potentially generate a permeability network throughout the subduction
606 system, with efficient transport along the deformation zone, and more limited one across it.
607
608 5. Conclusions
609 This work presents detailed microstructural observations to determine the mode of
610 deformation in both experimentally and naturally deformed samples at subduction conditions,
611 and near antigorite breakdown. Our results show that:
612 - Antigorite deforms in the semibrittle regime at high pressure. Brittle deformation in
613 subduction zones is likely associated with high strain-rate events, including seismic events
614 and can overimprint low strain-rate plastic deformation microstructures.
615 - The relative importance of brittle deformation relative to plastic deformation is likely
616 promoted by a combination of the presence of water (elevated pore fluid pressures and
617 dehydration), higher temperature and elevated strain rates.
618 - The crystal lattice structure of antigorite favours microcracking along (001), which promotes
619 interconnected porosity along the foliation direction in subduction zones. Antigorite structure
620 also induces significant intragranular fracturing. Semibrittle deformation can thus sustain a
621 permeable deformation zone down to the level of antigorite dehydration.

- Owing to a likely anisotropic permeability network, aqueous fluids may migrate more efficiently along the surface of the subducting slab than across it, exploiting the microporosity developed along the foliation during brittle deformation events. Across-deformation zone migration may be facilitated through intragranular fracturing, resulting in an upward migration towards the mantle wedge above the subduction plane allowing its hydration.

Acknowledgements: The authors wanted to thank J.A. Padrón-Navarta and a second reviewer for their great work reviewing this manuscrit. We are also grateful to the BGI Bayreuth technical staff for assistance with the preparation of the recovered samples. This work was supported by PNP and SYSTER Program (INSU/CNRS) and BGI "IHP Access to Research Infrastructure program. G. Hirth was supported by National Science Foundation grant EAR-0810188 for experiment W1460 used in this study.

637 **Table 1** : Experimental conditions for D-DIA and Griggs runs, and metamorphic conditions
638 undergone by natural samples

Experimentally-deformed serpentinites						
Sample	P (Gpa)*	T (°C)*	Strain rate	Total strain	dehydration evidence	Ref
DD60	1.0	400	5×10-5	24%	none	This study
DD61	1.0	400	1×10-4	26%	none	This study
DD63	1.8	550	-	static	none	This study
DD64	1.8	550	1×10-4	28%	none	This study
DD65	1.8	550	5×10-5	27%	none	This study
DD58	2.5	650	1×10-5	8%	olivine	This study
DD59	2.5	650	1×10-4	26%	olivine	This study
DD66	3.5	650	5×10-5	30%	olivine	This study
W1460	1.0	400	1.5×10-5	33%	none	Chernak et al, 2010

Naturally sheared serpentinites					
Sample	P (GPa)	T (°C)	Origin	dehydration evidence	Ref
Cu12 / Cu24	1.2 ± 2	450 ± 30	Escambray, Cuba	none	Auzende et al, 2004
Al24 (ET1)	0.9 ± 3	360 ± 60	Erro Tobbio, Alps	none	Hermann et al, 2000
Al19 / Al20 (ET3)	2.0 ± 2	600 ± 40	Erro Tobbio, Alps	ol + TiCl	Hermann et al, 2000

639 * errors are estimated according to Wang et al (2003) - T ± 20°C, P ± 10%

640

641

642

643

644

645

646 **Table 2** : Description of the deformation-linked microstructures observed in antigorite
647 serpentinites (from Otten, 1993; Gorbety, 2003; Passchier & Trouw, 2005)

648

Type of microstructure	Abbreviation	Description
Decompression cracks	Decomp.	Cracks due to the decompression of the assembly after temperature quench
Shear band	SB	Wavy ductile structure which localize intense strain. Common in phyllites
Kink band	KB	Tabular fold zones due to slipping of basal planes and resulting from shear couple
Microcracks	µC	Brittle planar discontinuity, commonly with some dilatation. High density of microcracking can lead to through-going fault
Dislocation wall	DW	Intracrystalline planar zone that concentrate migrating dislocations. Can evolve to a neoformed grain boundary (GB)
Offset	O	Lateral gliding of the layers (along *a*) due to the shift of the tetrahedral reversal from TO layer to the other by one tetrahedron position
Twinning	Tw	Mirror operation along the basal plane coupled to a gliding of the layer of *a*/2. The modulations are thus shifted of half a wavelenght
Two-layer polytype	2L-P	Combination of twining or offset can lead to a 1.4 nm periodicity in the c* direction instead of 0.7 nm typical of antigorite
Stacking defect	SD	All other possible types of stacking defects (or unrecognized)
Modulation dislocation	MD	Termination of antigorite waves on modulation dislocations.
Recrystallisation	R	Zones of recrystallisation attributed to pressure solution processes

649

650

Figure captions

Figure 1 : P-T diagram plotting the experimental conditions reported in this study and from previous experimental works. Curve limiting the thermal stability of antigorite are reported from Ulmer & Trommsdorff (1999) and Hilairet et al (2006). We also reported the curve from Ulmer & Trommsdorff (1995) which is widely used in the litterature but is incorrect (see Ulmer & Trommsdorff, 1999). We also plotted the metamorphic conditions undergone by natural samples (ET1, 2 and 3 correspond to Erro-Tobbio metamorphic stages from Hermann et al, 2000; VM, PG and LG stand for Vizzo Mozzo, Passo Gallarino and Lago Superiore units described by Schwartz et al, 2000) as well as experimental conditions from previous studies. Insert illustrates to the corrugated crystal structure of antigorite (dark silicate tetrahedra and light magnesian octahedra)

Figure 2. a) schematic representation of the assembly prepared for the D-DIA experiment, and b) photography of the assembly, c) the assembly monted in the D-DIA, d) optical microscopy image of a recovered sample (DD59)

Figure 3. a) Starting material image under cross polarized light showing interpenetrative texture of antigorite (Atg) serpentininite, b) TEM micrograph of crosscutting antigorite blades from the starting material. c) natural light / cross polarized light mounted image of sample DD63 (static run) showing decompression-induced fractures (Decomp). $\sigma 1$ is horizontal.

Figure 4. Optical microphotographs of recovered samples from non-dehydrated and dehydrating experiments. $\sigma 1$ is vertical on all images except b where it is rotated of 90°. a) typical interpenetrative texture inherited from the starting material (DD65), b) oblique localized damaged zone crosscutting the sample (DD61), c) fault crosscutting W1460 (Chernak et al, 2010), d) Secondary micrograins of olivine associated to antigorite underline the significant dehydration of DD66, e) dehydrated samples showing local concentration of inframicronic grains of olivine (showed by blue arrows) (DD59).

Figure 5. TEM bright field microcrographs of recovered samples from non-dehydrated experiments. a) and b) show catactlastic textures with antigorite grains cracking preferentially along (001) cleavage (Cl), c) intracrystalline microcracks propagating through an antigorite crystal. Antigorite lamellae can be recognized, d, e and f) antigorite crystal showing kink

684 bands (KB), with a gliding of the basal planes along *a* direction (d and e) and b (f). Antigorite
685 shown on f) is observed along <100) and can be discriminated from lizardite on SAED pattern
686 by slight tilting the crystal and revealing surstructure diffration spots (DW = dislocation wall),
687 g) bright field and associated SAED pattern of an ordered antigorite, h) bright field and
688 associated SAED pattern of a slightly disordered antigorite showing twinning (Tw) and
689 stacking defects (SD).
690
691 **Figure 6.** TEM bright field microcrographs of recovered samples from dehydrating
692 experiments a) and associated SAED pattern showing olivine grains (Ol) decorating the edges
693 of a microcrack, b) and associated SAED pattern showing kinked antigorite, c) and associated
694 SAED pattern showing highly disordered antigorite. Staking disorder is emphasized on the
695 SAED pattern by the presence of diffuse streaks along c^*, d) antigorite crystal showing
696 migrating dislocation walls (DW) that may evolve to grain boundary (GB)
697
698 **Figure 7**. Optical microphotographs of naturally sheared serpentinite samples. a) antigorite
699 serpentinite Cu12 from the Escambray massif (Cuba). Foliation is underlined by slighthly
700 deformed antigorite blades, highly sheared antigorite mylonite from b) unit I of Erro Tobbio
701 (Alps) showing shear bands (SB), and c) from unit III of Erro Tobbio (Alps) showing
702 plurimicronic kink bands and veins filled with by products of antigorite dehydration olivine et
703 Titano-clinohumite
704
705 **Figure 8.** TEM bright field microcrographs of naturally sheared serpentinites showing a) high
706 intracrystalline disorder, as observed on the micrograph and associated SAED pattern, b) high
707 resolution image of a slightly disorder antigorite crystal with a modulation dislocation (D), c)
708 microcrack healed by recrystallisation (R) due to pressure solution, d) microcrack with little
709 recrystallisation, e) elongated antigorite blades, f) chrysotile veins inherited from the oceanic
710 event or produced during fluid migration in subduction context, g) antigorite seen along
711 <001> showing modulation dislocation
712
713 **Figure 9.** Schematic cartoon of a subduction zone (redrawn after Hilairet & reynard, 2009
714 and Kawano et al, 2011). Two isotherms are represented (1100 and 1400°C). The green
715 region correspond to the serpentinized mantle, the dotted line represent the antigorite
716 breakdown conditions and and the blue arrows represent the putative migration paths of the
717 fluids produced by sediment dehydration. Insert : Magnification of the serpentine channel

above the subducting slab. Fluids can migrate mostly paralelly to the foliation, promoting the formation of the serpentinized layer above the subducting slab. They can also migrate upwards and hydrate the mantle wedge and contribute to arc magmatism through intracrystalline microcracks.

REFERENCES

Agard, P., Yamato, P., Jolivet, L., Burov E., 2009. Exhumation of oceanic blueschists and eclogites in subduction zones: Timing and mechanisms. Earth Sci. Rev. 92, 53-79. DOI: 10.1016/j.earscirev.2008.11.002.

Amiguet, E., Van de Moortele, B., Cordier, P., Hilairet, N., Reynard, B., 2014. Deformation mechanisms and rheology of serpentines in experiments and in nature. J. Geophys. Res. 4640-4654.

Andreani, M., Mevel, C., Boullier, A-M., Escartin, J., 2007. Dynamic control on serpentine crystallization in veins: Constraints on hydration processes in oceanic peridotites. Geoch. Geophys. Geosyst. 8, Q02012. DOI: 10.1029/2006GC001373.

Angiboust, S., Langdon, R., Agard, P., Waters, D., Chopin, C., 2011. Eclogitization of the Monviso ophiolite and implications on subduction dynamics. J. Metam. Geol. 30, 37–61.

Auzende, A.L., Guillot, S., Devouard, B., Baronnet, A., 2006. Behaviour of serpentinites in convergent context : Microstructural evidence. Eur. J. Mineral. 18, 21-33.

Auzende, A-L., Daniel, I., Reynard, B., Lemaire, C., Guyot, F., 2004. High-pressure behaviour of serpentine minerals: a Raman spectroscopic study. Phys. Chem. Mineral. 31, 269-277. DOI 10.1007/s00269-004-0384-0.

Auzende, A-L., Devouard, B., Guillot, S., Daniel, I., Baronnet, A., Lardeaux, J-M., 2002. Serpentinites from Central Cuba: petrology and HRTEM study. Eur. J. Mineral. 14, 905-914.

Bezacier, L., Reynard, B., Bass, J., Sanchez Valle, C., van de Moortele, B., 2010. Elasticity of antigorite, seismic detection of serpentinites, and anisotropy in subduction zones. Earth Planet. Sci. Lett. 289, 198-208.

Chernak, L.J., Hirth, G., 2010. Deformation of antigorite serpentinite at high temperature and pressure. Earth Planet. Sci. Lett. 296, 23-33.

748 Chernak, L.J., Hirth, G., 2011. Syndeformational antigorite dehydration producesstable fault
749 slip. Geology 39, 847-850. doi:10.1130/G31919.1.

750 Christensen, N.I., 2004. Serpentinites, peridotites and seismology. Int. Geol. Rev. 46:795-816.

751 Deschamps, F., Godard, M., Guillot, S., Hattori, K.H., 2013. Geochemistry of subduction zones
752 serpentinites: A review. Lithos, doi: 10.1016/j.lithos.2013.05.019.

753 Dobson, D.P., Meredith, P.G., Boon, S.A., 2002. Simulation of subduction zone seismicity by
754 dehydration of serpentine. Science, 298, 407-1410.

755 Escartin, J., Hirth G., 1997. Non dilatant brittle deformation of serpentinites: Implications for
756 Mohr-Coulomb theory and the strength of faults. J. Geophys. Res. 102, 2897-2913.

757 Escartin, J., Andreani, M., Hirth, G., Evans, B., 2008. Relationships between the
758 microstructural evolution and the rheology of talc at elevated pressures and temperatures.
759 Earth Planet. Sci. Lett. 268, 463-475. DOI: 10.1016/j.epsl.2008.02.004.

760 Frey, M., Robinson, D., 1999. Low grade metamorphism. Backwell Sci Ltd pp313.

761 Fryer, P., Wheat, C.G., Mottl, M.J., 1999. Mariana blueschist mud volcnism: Implications for
762 conditions within the subduction zone. Geology 27, 103-1999. DOI: 10.1130/0091-
763 7613(1999)027<0103:MBMVIF>2.3.CO;2.

764 Garth, T., Rietbrock, A., 2014. Order of magnitude increase in subducted H2O due to
765 hydrated normal faults within the Wadati-Benioff zone. Geology 42, 207–210.

766 Grobety, B., 2003. Polytypes and higher-order structures of antigorite : A TEM study. Am
767 Mineral 88, 27-36.

768 Guillot, S., Agard, P., Schwartz, S., Vidal, O., 2009. Exhumation processes in oceanic and
769 continental subduction contexts: A review In: Lallemand S, Funiciello F (Eds) Frontiers in
770 Earth Science, 175-205. doi: 10.1007/978-3-540-87974-9_10.

771 Guillot, S., Hattori, K.H., de Sigoyer, J., Nagler, T., Auzende, A.L., 2001. Evidence of
772 hydration of the mantle wedge and its role in the exhumation of eclogites. Earth Planet.
773 Sci. Lett. 193, 115-127.

774 Hacker, B.R., Peacock, S.M., Abers, G.A., Holloway, S.D., 2003. Subduction factory - 2. Are
775 intermediate-depth earthquakes in subducting slabs linked to metamorphic dehydration
776 reactions? J. Geophys. Res. 108:B1203. DOI: 10.1029/2001JB001129.

777 Hirauchi, K.I., Katayama, I., Uheara, S., Miyahara, M., Takai, Y., 2010. Inhibition of
778 subduction thrust earthquakes by low temperature plastic flow in serpentine. Eart Planet. Sci.
779 Lett. 295, 349-357. DOI: 10.1016/j.epsl.2010.04.007
780 Hirth, G., Guillot, S., 2013. Rheology and tectonic significance of serpentinite. Elements 9.
781 doi: 10.2113/gselements.9.2.95.

782 Hermann, J., Müntener, O., Scambelluri, M., 2000. The importance of serpentine mylonites
783 for subduction and exhumation of oceanic crust. Tectonophysics 327, 225-238.

784 Hilairet. N., Daniel, I., Reynard, B., 2006. Equation of state of antigorite, stability field of
785 serpentines, and seismicity in subduction zones. J. Geophys. Res. 83: L02302.
786 doi:10.1029/2005GL024728.

787 Hilairet, N., Reynard, B., 2009. Stability and dynamics of serpentinite layer in subduction
788 zone. Tectonophysics 465, 24-29. DOI: 10.1016/j.tecto.2008.10.005.

789 Hilairet, N., Reynard, B., Wang, Y., Daniel., I, Merkel, S., Nishiyama, N., Petitgirard, S.,
790 2007. High-pressure creep of serpentine, interseismic deformation and initiation of
791 subduction. Science 318, 1910-1913.

792 Hyndman, R.D., Peacock, S.M., 2003. Serpentinization of the forearc mantle. Earth Planet.
793 Sc. Lett. 212, 417-432.

794 Jung, H., Karato, S., 2001. Water induced fabric transitions in olivine. Science 293, 1460-
795 1463.

796 Jung, H., Green, H.W., Dobrzhinetskaya, F., 2004. Intermediate-depth earthquake faulting by
797 dehydration embrittlement with negative volume change. Nature 428, 545-549

798 Jung, H., Green, H.W., 2004. Experimental Faulting of Serpentinite duringDehydration:
799 Implications for earthquakes, Seismic Low-Velocity Zones, and Anomalous Hypocenter
800 Distributions in Subduction Zones. Internat. Geol. Rev. 46, 1089-1102.

801 Jung, H., Fei, Y., Silver, P., Green, H.W., 2009). Frictional sliding in serpentine at very high
802 pressure: Earth Planet. Sci. Lett. 277: 273–279, doi:10.1016/j.epsl.2008.10.019.
803 Kamiya, S., Kobayashi, Y., 2000. Seismological evidence for the existence of serpentinized
804 mantle wedge. Geophys. Res. Lett. 27, 819-822.

805 Katayama, I., Hirauchi, K.I., Michibayashi, K., Ando, J.I., 2009. Trench-parallel anisotropy
806 produced by serpentine deformation in the hydrated mantle wedge. Nature 461, 1114-1117
807 Kawano, S., Katayama, I., Okazaki, K., 2011. Permeanility anisotropy of serpentinite and
808 fluid pathways in subduction zones. Geology 39, 939-942.

809 Kunze, G., 1956. Die gewellte struktur des antigorits, I. Zeitsch Kristall 108, 82-107.

810 Marchesi, C., Garrido, C.J., Padrón-Navarta, J.A., López Sánchez-Vizcaíno, V., Gómez-
811 Pugnaire, M.T., 2013. Element mobility from seafloor serpentinization to high-pressure
812 dehydration of antigorite in subducted serpentinite: Insights from the Cerro del Almirez
813 ultramafic massif (southern Spain). Lithos 15, 128-142.

814 Mei, S., Kohlstedt, D.L., 2000a. Influence of water on plastic deformation of olivine
815 aggregates. 1. Diffusion creep regime. J. Geophys. Res. 105, 21457-21469

816 Mei, S., Kohlstedt, D.L., 2000b. Influence of water on plastic deformation of olivine
817 aggregates. 2. Dislocation creep regime. J. Geophys. Res. 105, 21471-21481

818 Mellini, M., 1982. The crystal structure of lizardite-1T: hydrogen bonds and polytypism. Am.
819 Mineral. 67, 587-598.

820 Mevel, C., 2003. Serpentinization of abyssal peridotites at mid-ocean ridges. C. R. Geosc.
821 335, 825-852.

822 Omori, S., Komobayashi, T., Maruyama, S., 2004. Dehydration and earthquakes in the
823 subducting slab: empirical link in intermediate and deep seismic zones. Phys. Earth
824 Planet. Int. 146, 297-311.

825 Otten, M.T., 1993. High-resolution transmission electron-microscopy of polysomatism and
826 stacking defects in antigorite. Am. Mineral. 78,75-84.

827 Padrón-Navarta, J.A., Tommasi, A., Garrido, C.J., Lopez Sanchez, V., 2012. Plastic
828 deformation and development of antigorite crystal preferred orientation in high-pressure
829 serpentinites. Earth Planet. Sci. Lett. 349-350, 75-86.

830 Padrón-Navarta, J.A., Tommasi, A., Garrido, C.J., Lopez Sanchez, V., Gomez-Pugnaire,
831 M.T., Jabaloy, A., Vauchez, A., 2010. Fluid transfer into the wedge controlled by high-
832 pressure hydrofracturing in the cold top-slab mantle. Earth Planet. Sci. Lett. 297, 271-286.

833 Padrón-Navarta, J.A., López Sánchez-Vizcaíno, V., Garrido, C.J., Gómez-Pugnaire, M.T.,
834 Jabaloy, A., Capitani, G., Mellini, M., 2008. Highly ordered antigorite from Cerro del

835 Almirez HP-HT serpentinites, SE Spain. Contributions to Mineralo gy and Petrology 156,
836 679-688

837 Passchier, C.W., Trouw, R.A., 2005. Microtectonics, Springer, Berlin

838 Paterson, M.S., Weiss, L.E., 1966. Experimental deformation and folding in phyllite. Geol.
839 Soc. Am. Bull. 77, 343-374. DOI: 10.1130/0016-7606(1966)77[343:EDAFIP]2.0.CO;2

840 Peacock, S.M., 2001. Are the lower planes of double seismic zones caused by serpentine
841 dehydration in subducting oceanic mantle. Geology, 29, 299-302.

842 Perrillat, J.P., Daniel, I., Koga, K.T., Reynard, B., Cardon, H., Crichton, W.A., 2005. Kinetics
843 of antigorite dehydration: A real-time diffraction study. Earth Planet. Sci. Lett. 236, 899-
844 913. DOI: 10.1016/j.epsl.2005.06.006.

845 Reynard, B., 2013. Serpentine in active subduction zones. Lithos 178, 171-185.

846 Scambelluri, M., Muntener, O., Hermann, J., Piccardo, G.B., Trommsdorff, V. (1995)
847 Subduction of water into the mantle: history of an alpine peridotite. Geology 23, 459–
848 462.

849 Schmidt, M.W., Poli, S., 1998. Experimentallu based water budgets for dehydrating slabs and
850 consequence for arc magma generation. Earth Planet. Sci. Lett. 163, 361-379. DOI:
851 10.1016/S0012-821X(98)00142-3.

852 Schwartz, S., Lardeaux, J.M., Guillot, S., 2000. The diversity of eclogitic metamorphism in
853 the Monviso ophiolitic complex, western Alps, Italy. Geodyn. Acta. 13, 169-188.

854 Shea, W.T., Kronenberg, A.K., 1992. Rheology and deformation mechanisms of an isotropic
855 mica schist. J. Geophys. Res. 97, 15201-15237.

856 Spear, F.S., 1995. Metamorphic Phase Equilibria and Pressure-Temperature-Time Paths.
857 Mineral. Soc. Am., Mon Ser pp799.

858 Tatsumi, Y., Kogiso, T., 2003. The subduction factory: Its role in the evolution of the earth's
859 crust and mantle. Geol. Soc. London Spec. publ. 2003 219:55-80. doi:
860 10.1144/GSL.SP.2003.219.01.03.

861 Ulmer. P., Trommsdorff, V., 1999. Phase relations of hydrous mantle subducting to 300 km,
862 in: Fei Y, Bertka CM, Mysen BO (Eds) Mantle Petrology: Field observations and high
863 pressure experimentations. The Geochemical Society, pp259-281.

Ulmer, P., Trommsdorff, V., 1995. Serpentine stability to mantle depths and subduction-related magmatism. Science 268, 858-861.

van de Moortele, B., Bezacier, L., Trullenque, G., Reynard, B., 2010. Electron back-scattering diffraction (EBSD) measurements of antigorite lattice-prefefred orientations (LPO). J. Microsc. 239, 245-248.

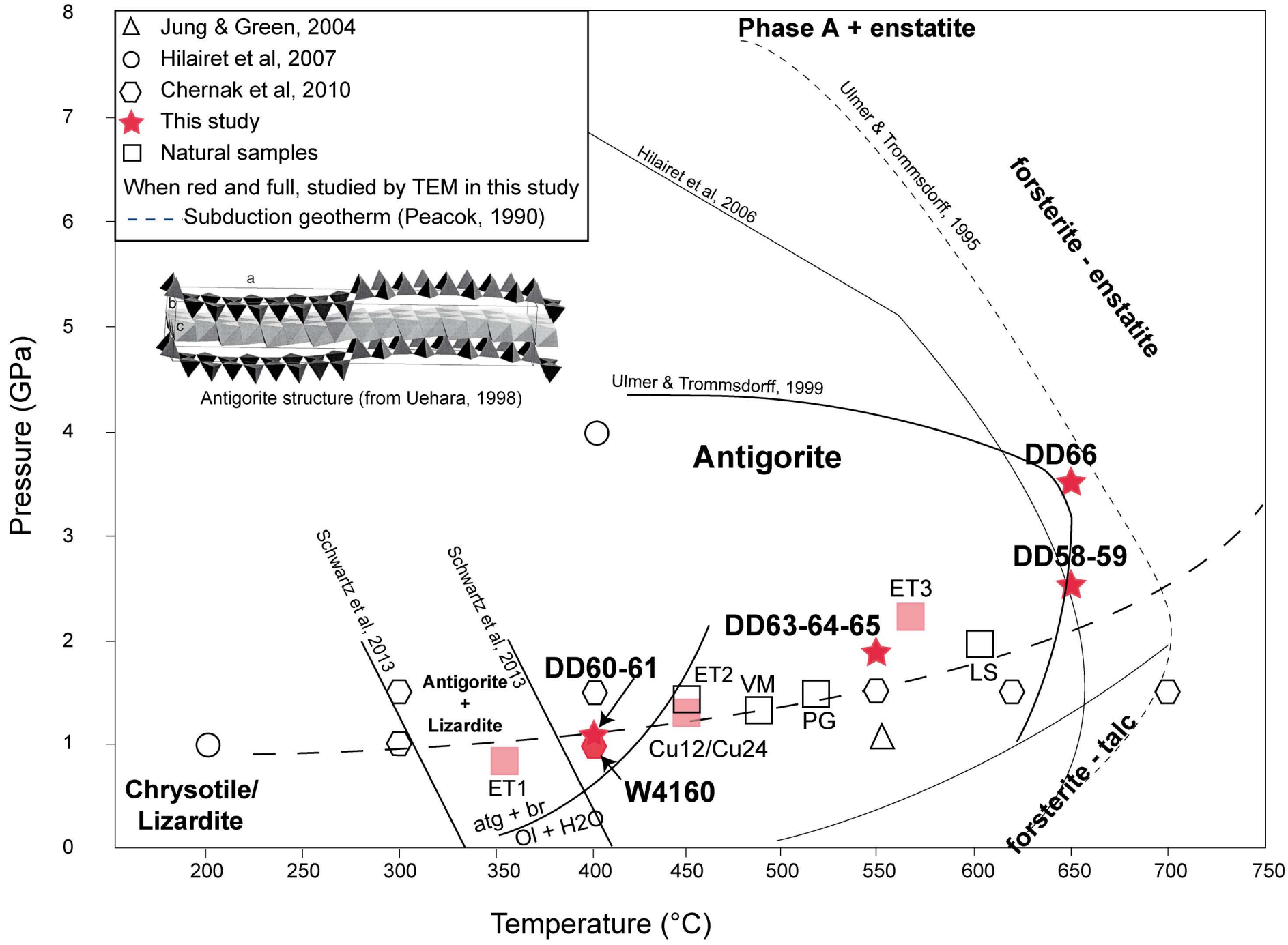
van Keken, P., 2003. The structure and dynamics of the mantke wedge. Earth Planet. Sci. Lett. 215, 323-338.

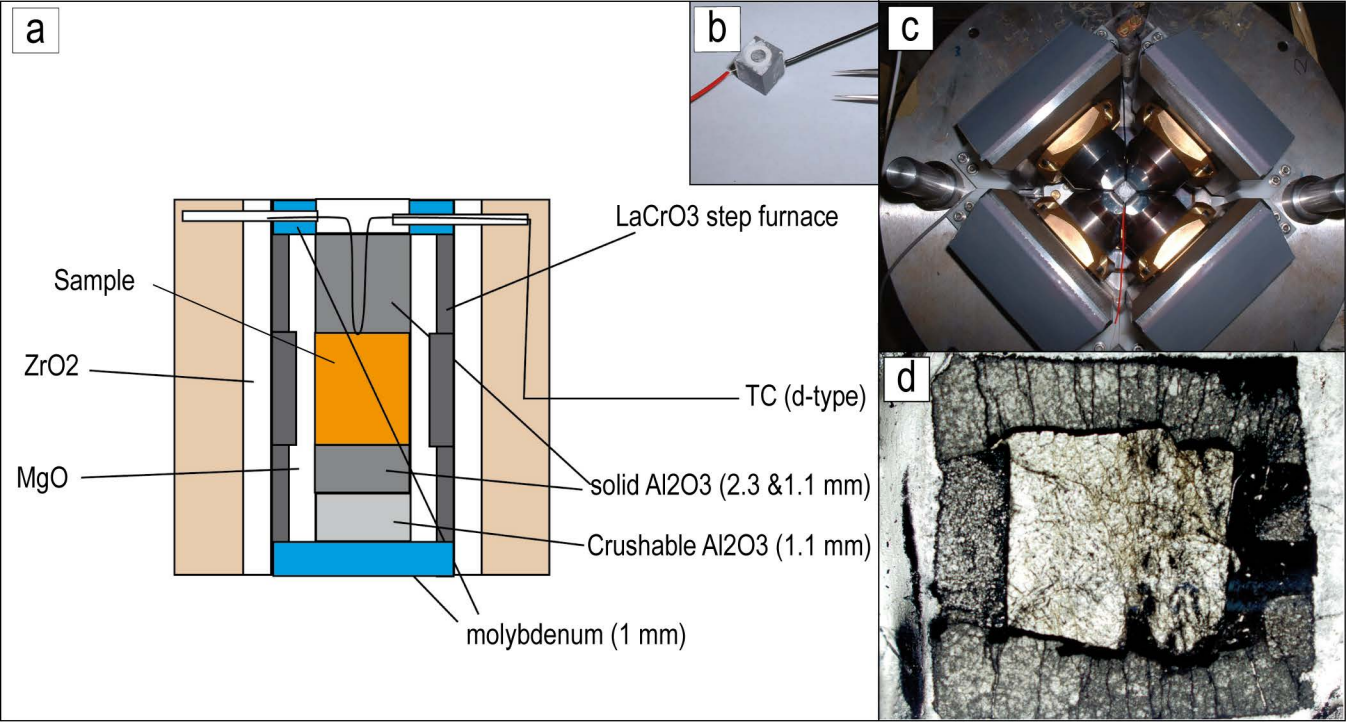
Viti, C., Hirose, T., 2009. Dehydration reactions and micro/nanostructures in experimentally-deformed serpentinites. Contrib. Mineral. Petrol. 157, 327-338.

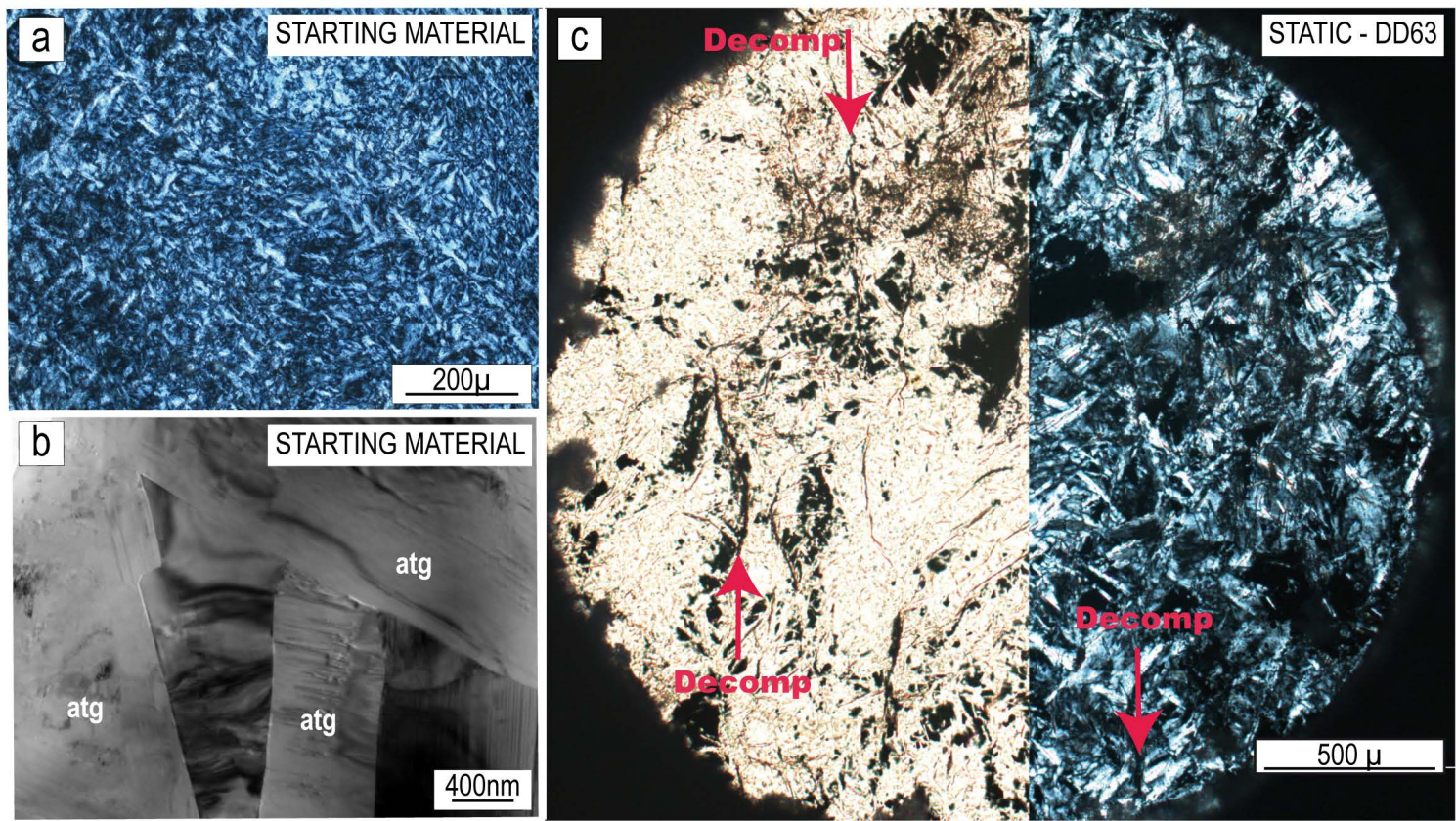
von Mises, R., 1928. Mechanics of the ductile form changes of crystals. Zeits. Angewan. Math. Mech. 8, 161-185.

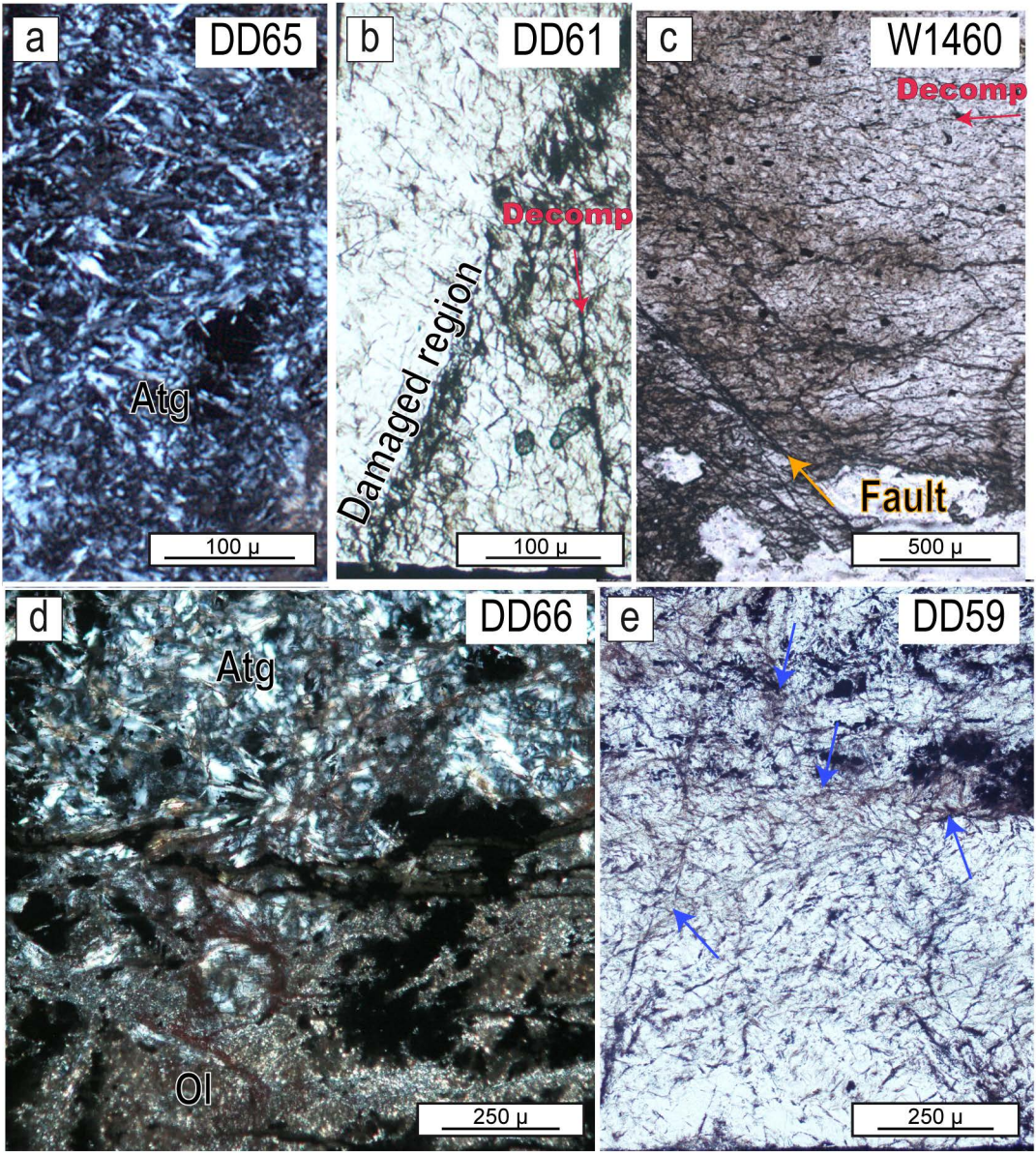
Wada, I., Wang, K., He, J., Hyndman, R., 2008. Weakening of the subduction interface and its effects on surface heatflow, slab dehydration, and mantle wedge serpentinization. J. Geophys. Res. 113, B04402. doi:10.1029/2007JB005190.

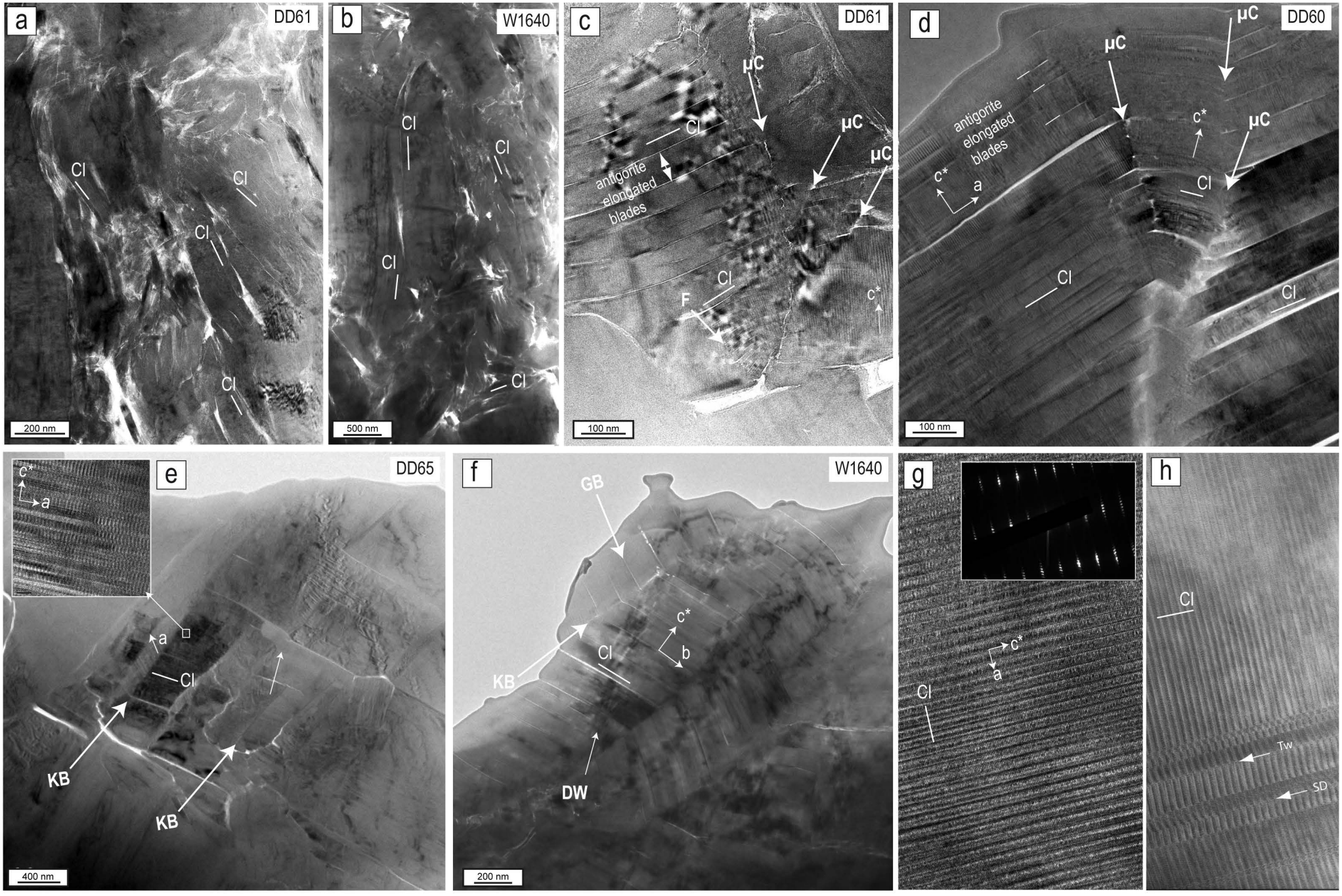
Wang, Y., Durham, W.B., Getting, I.C., Weidner, D.J., 2003. The deformation-DIA: A new apparatus for high temperature triaxial deformation to pressures up to 15 GPa. Rev. Sci. Instrum. 74, 3002-3011.

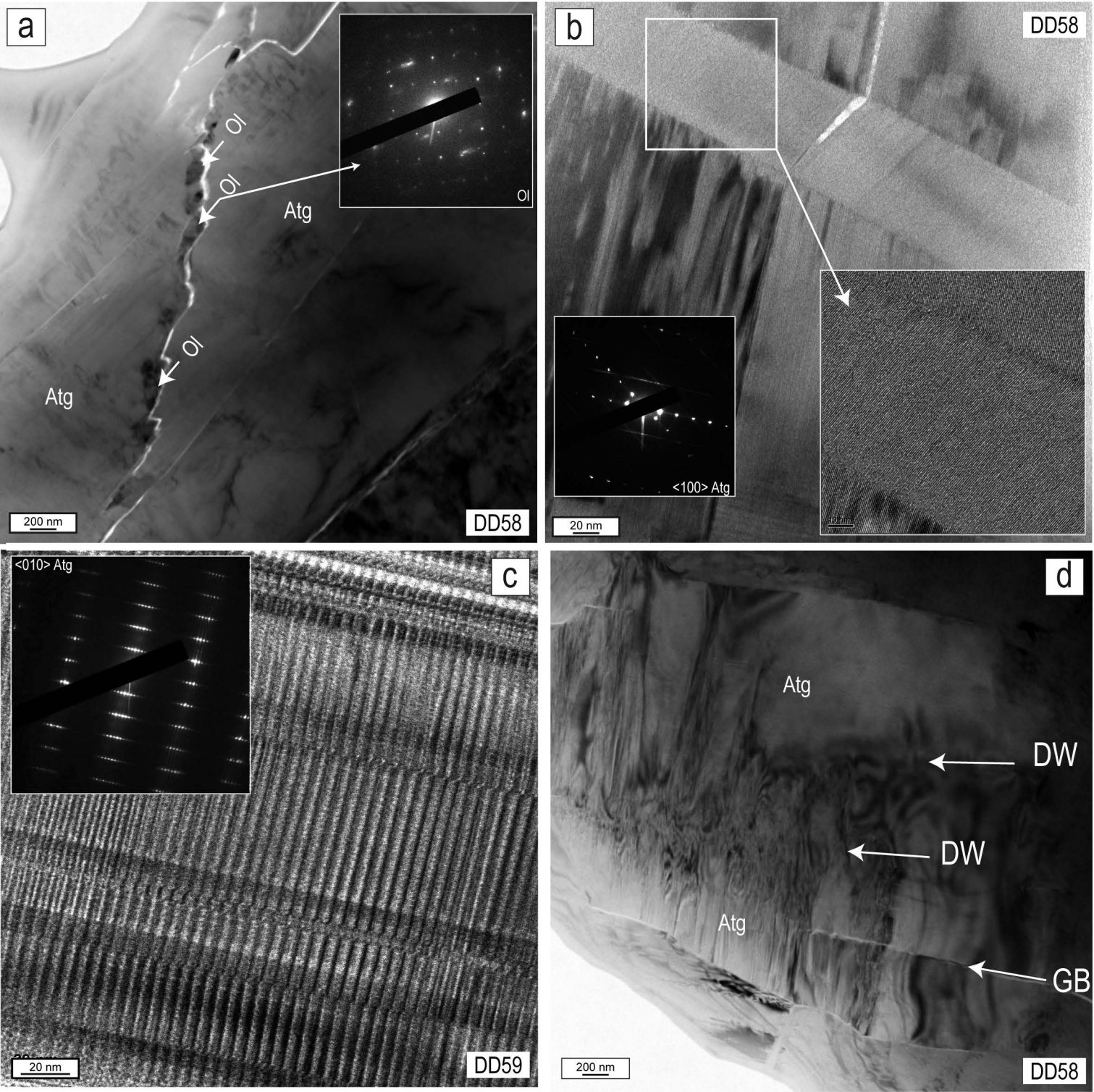

Jung & Green, 2004
Hilairet et al, 2007
Chernak et al, 2010
This study
Natural samples
When red and full, studied by TEM in this study
Subduction geotherm (Peacok, 1990)
Antigorite structure (from Uehara, 1998)
Phase A + enstatite
Ulmer & Trommsdorff, 1995
Hilairet et al, 2006
forsterite - enstatite
Ulmer & Trommsdorff, 1999
Antigorite
DD66
DD58-59
DD63-64-65
ET3
DD60-61
ET2
VM
PG
LS
Cu12/Cu24
W4160
ET1
Antigorite + Lizardite
Chrysotile/ Lizardite
Schwartz et al, 2013
Schwartz et al, 2013
atg + br
Ol + H2O
forsterite - talc
Pressure (GPa)
Temperature (°C)
0
1
2
3
4
5
6
7
8
200
250
300
350
400
450
500
550
600
650
700
750

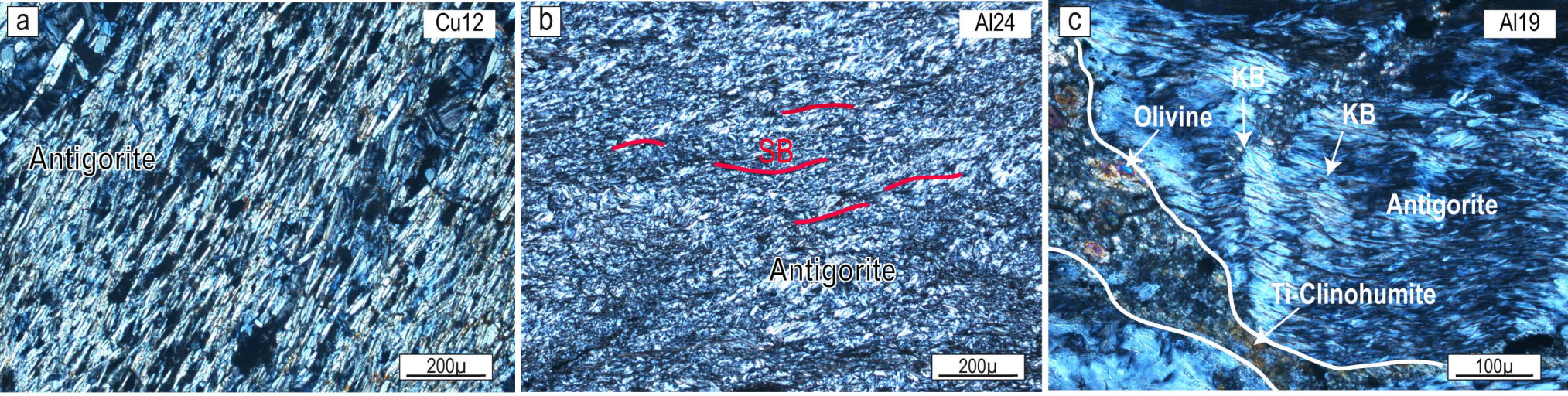

a
b
c
d
LaCrO3 step furnace
Sample
ZrO2
TC (d-type)
MgO
solid Al2O3 (2.3 &1.1 mm)
Crushable Al2O3 (1.1 mm)
molybdenum (1 mm)

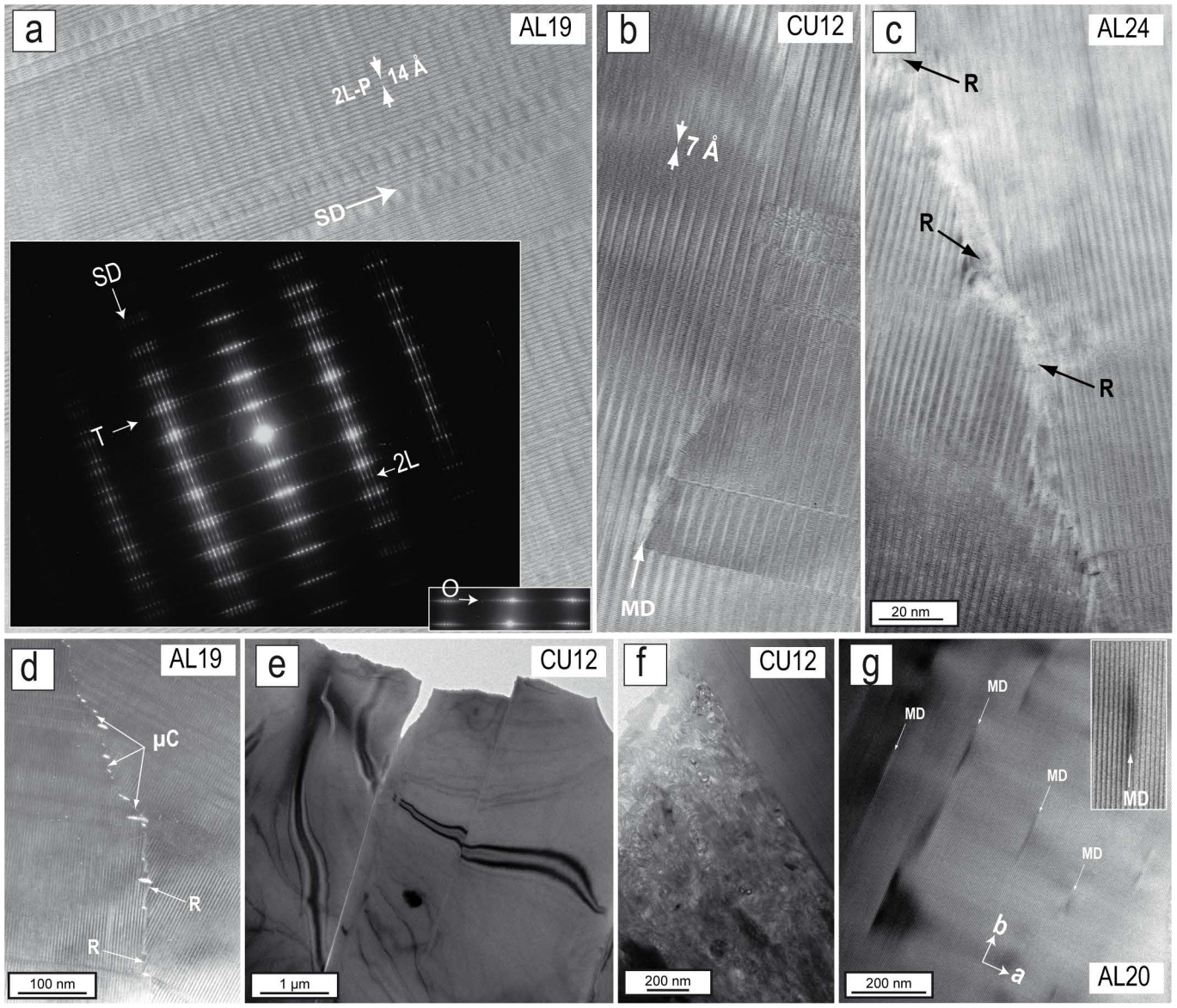

a
STARTING MATERIAL
200µ
b
STARTING MATERIAL
atg
atg
atg
400nm
c
Decomp
Decomp
STATIC - DD63
Decomp
500 µ

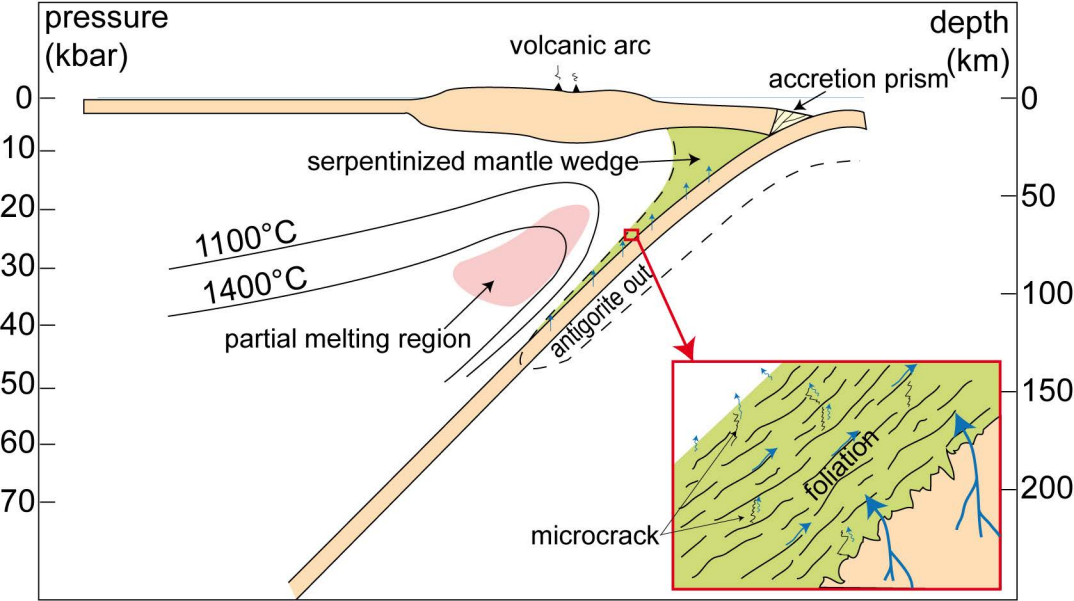

a
DD65
Atg
100 µ
b
DD61
Decomp
Damaged region
100 µ
c
W1460
Decomp
Fault
500 µ
d
DD66
Atg
Ol
250 µ
e
DD59
250 µ


a
DD61
Cl
Cl
Cl
Cl
200 nm
b
W1640
Cl
Cl
Cl
Cl
500 nm
c
DD61
μC
μC
μC
Cl
antigorite elongated blades
Cl
F
c*
100 nm
d
DD60
μC
μC
μC
antigorite elongated blades
c*
a
c*
Cl
Cl
Cl
100 nm
e
DD65
c*
a
a
Cl
KB
KB
400 nm
f
W1640
GB
c*
b
Cl
KB
DW
200 nm
g
c*
a
Cl
Cl
h
Cl
Tw
SD


a
Ol
Ol
Atg
Ol
Atg
Ol
200 nm
DD58
b
DD58
<100> Atg
20 nm
c
<010> Atg
20 nm
DD59
d
Atg
DW
DW
Atg
GB
200 nm
DD58


a
Cu12
Antigorite
200µ
b
Al24
SB
Antigorite
200µ
c
Al19
KB
KB
Olivine
Antigorite
Ti-Clinohumite
100µ


a
AL19
2L-P
14 Å
SD
SD
T
2L
O
b
CU12
7 Å
MD
c
AL24
R
R
R
20 nm
d
AL19
μC
R
R
100 nm
e
CU12
1 μm
f
CU12
200 nm
g
MD
MD
MD
MD
MD
b
a
200 nm
AL20


pressure
(kbar)
depth
(km)
volcanic arc
accretion prism
0
10
20
30
40
50
60
70
0
50
100
150
200
serpentinized mantle wedge
1100°C
1400°C
partial melting region
antigorite out
foliation
microcrack